51st AIAA Aerospace Sciences Meeting including the New Horizons Forum and Aerospace Exposition
07 - 10 January 2013, Grapevine (Dallas/Ft. Worth Region), Texas

AIAA 2013-0010

Prediction of Jet Noise Shielding with Forward Flight Effects

Salvador Mayoral* and Dimitri Papamoschou†
University of California, Irvine, Irvine, CA, 92697, USA

Use of conventional scattering solvers for the problem of sound diffraction in the presence of a mean flow requires the use of variable transformations that reduce the wave equation to its canonical form. This enables the assessment of the mean-flow impact on the radiation of the isolated source as well as its diffraction by an object. Applications include the shielding of propulsion noise sources by the airframe. The focus of this study is the diffraction of a wavepacket noise source, simulating jet noise, from a surface having the general shape of the hybrid-wing-body (HWB) airplane. In addition, the canonical problem of monopole diffraction by a sphere is addressed. In both instances the potential solution for the mean flow is used in the transformations, and the boundary element method is used to compute the scattered fields. The study addresses the effect of the mean flow on the incident and total pressure fields and conducts a systematic assessment of the errors introduced by the transformations. The general trend is a compaction of the downstream influence of the noise source, leading to better shielding for the HWB problem. The overall error tends to be less than 5% for flight Mach number not exceeding 0.2.

Nomenclature

D_j	=	jet diameter
E, E'	=	error field
a	=	speed of sound
f	=	cyclic frequency
k	=	acoustic wavenumber $= \omega/a_\infty$
k_x	=	axial wavenumber
k_r	=	radial wavenumber
M	=	Mach number
$\mathbf{n}$	=	unit normal
p	=	pressure
r	=	radial distance in polar or spherical coordinate systems
s	=	wing span
Sr	=	Strouhal number
t	=	time
$\mathbf{u}$	=	velocity vector
U_j	=	jet velocity
$\mathbf{x} = (x, y, z)$	=	position vector
θ	=	polar angle relative to downstream axis
ψ	=	azimuth angle
ϕ	=	perturbation velocity potential
ρ	=	density
ω	=	angular frequency

*Graduate Student Researcher, Department of Mechanical Aerospace Engineering, Member AIAA
†Professor, Department of Mechanical and Aerospace Engineering, Fellow AIAA

Subscripts

∞	=	freestream
i	=	incident field
s	=	scattered field
t	=	total field

Modifiers

$\bar{(\,)}$	=	mean component
$(\,)'$	=	acoustic fluctuation component
$\widehat{(\,)}$	=	axial Fourier transform
$\widetilde{(\,)}$	=	transformed domain

I. Introduction

The acoustics of airframe-propulsion integration are gaining attention as aircraft design is increasingly being driven by low-noise considerations. Accurate and efficient prediction tools that can provide design guidance for conventional and advanced aircraft are sought out. An example low-noise configuration is the hybrid-wing-body (HWB) airplane where the engines are mounted on top of the airframe. The airframe can thus be used to "shield" the power-plant noise emitted towards communities. The prediction approach requires efficient computational methods in conjunction with practical but realistic formulations of the noise sources. The sources are generally very complex and defy a prediction approach from first principles. Approximate, physical models are needed that capture the salient features of the noise sources without imposing excessive computational demands.

Scattering prediction tools include the boundary element method (BEM) and the method of equivalent sources, the latter implemented in the Fast Scattering Code (FSC).[1] These methods solve the canonical wave equation in the time domain or the canonical Helmholtz equation in the frequency domain. Thus they are limited to acoustic propagation in a homogeneous medium at rest. While this is useful for many applications, aircraft are inherently in motion and predictions of scattering with forward flight effects are critical. Formulations that solve directly the acoustic field, and its scattering, in a moving medium involve the solution of the linearized Euler or Navier-Stokes equations.[2] This is a very complex and computationally demanding approach that lacks the elegance and robustness of the BEM or FSC methods. A prediction tool based on the linearized Euler or Navier-Stokes equations is not on the horizon for the foreseeable future.

An alternative approach is to utilize transformations of the linearized equations that reduce them to the canonical wave equation. The traditional scattering methods would then be used in the transformed domain. Such transformation methods exist for uniform subsonic mean flow and for low-Mach number potential mean flow. In this report we examine the diffraction of sound in a potential flow field; a companion paper addresses noise sources and their diffraction with uniform flow.[3] The emphasis here is on the wavepacket noise source, which simulates jet noise emission, and its diffraction by a HWB-shaped boundary. It follows past work that predicted jet noise diffraction using a wavepacket model at static conditions.[4] We present the methodology for the transformation, treatment of the wavepacket source, computation of the potential mean flow, evaluation of errors inherent in the approximations, and sample results on the effect of mean flow on the diffraction. In addition, results from the benchmark problem of monopole diffraction by a sphere are presented. Even though the theoretical background of the governing equations and their transformation has been covered in past publications[5,6] we present a concise review of the analysis for completeness.

II. Theoretical Background

We develop the relations for the propagation of sound in an irrotational, homentropic, subsonic medium. The problem setup is illustrated in Fig. 1. The sound source could be external or the body itself (e.g., an aircraft surface that vibrates). The total velocity of the medium (mean plus acoustic) is expressed in terms of a velocity potential Φ,

$$\mathbf{u} = \nabla\Phi, \tag{1}$$

and thus satisfies automatically the irrotationality condition. In the development that follows D/Dt is the material derivative based on the total flow velocity and $\overline{D}/Dt$ is the material derivative based on the mean (steady) velocity component.

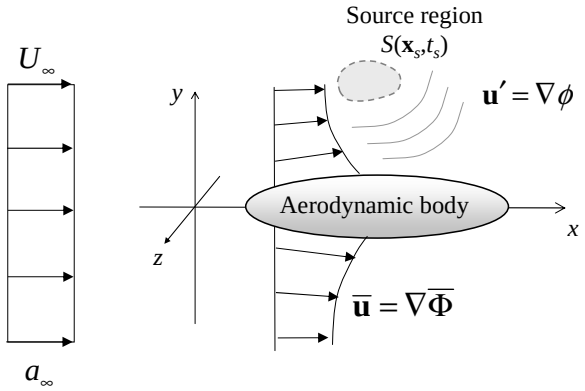

Figure 1. Acoustic propagation in a subsonic potential flow.

A. Governing Equations

The flow field being irrotational and homentropic, we invoke the unsteady Bernoulli equation

$$\frac{\partial\Phi}{\partial t} + \frac{1}{2}\mathbf{u}\cdot\mathbf{u} + \frac{a^2}{\gamma-1} \;=\; \frac{a_0^2}{\gamma-1} \tag{2}$$

where the relation $p/\rho = a^2/(\gamma-1)$ was used, with a_0 the total (reservoir) speed of sound. Applying the isentropic relation $\rho \sim a^{2/(\gamma-1)}$ to the continuity equation $D\rho/Dt = -\rho\nabla\cdot\mathbf{u}$ we obtain

$$\frac{1}{\gamma-1}\frac{Da^2}{Dt} = -a^2\nabla^2\Phi \tag{3}$$

The above two equations are combined by taking the total derivative of Eq. 2 and inserting the result of Eq. 3:

$$\frac{\partial^2\Phi}{\partial t^2} + 2\mathbf{u}\cdot\nabla\left(\frac{\partial\Phi}{\partial t} + \frac{1}{4}\mathbf{u}\cdot\mathbf{u}\right) - a^2\nabla^2\Phi = 0 \tag{4}$$

with

$$a^2 \;=\; a_0^2 - (\gamma-1)\left(\frac{\partial\Phi}{\partial t} + \frac{1}{2}\mathbf{u}\cdot\mathbf{u}\right) \tag{5}$$

The system of Eqs. 4 and 5 is exact for potential flow. Next we seek approximations for the acoustic field.

B. Decomposition

The flow field is decomposed into a mean potential part and an acoustic fluctuation according to

$$\nabla\Phi(\mathbf{x},t) \;=\; \overline{\mathbf{u}}(\mathbf{x}) + \nabla\phi(\mathbf{x},t) \tag{6}$$

where ϕ is the acoustic velocity potential. The same decomposition is applied to the square of the speed of sound:

$$a^2(\mathbf{x},t) = \overline{a^2}(\mathbf{x}) \;+\; (a^2)'(\mathbf{x},t) \tag{7}$$

Substituting in Eq. 4,

$$\frac{\partial^2\phi}{\partial t^2} + 2(\overline{\mathbf{u}}+\nabla\phi)\cdot\nabla\left(\frac{\partial\phi}{\partial t} + \frac{1}{4}\overline{\mathbf{u}}\cdot\overline{\mathbf{u}} + \frac{1}{2}\overline{\mathbf{u}}\cdot\nabla\phi + \frac{1}{4}|\nabla\phi|^2\right) - [\overline{a^2} + (a^2)']\nabla\cdot(\overline{\mathbf{u}}+\nabla\phi) = 0 \tag{8}$$

The mean component of Eq. 8 is the mechanical energy equation

$$\overline{\mathbf{u}} \cdot \nabla \left(\frac{1}{2} \overline{\mathbf{u}} \cdot \overline{\mathbf{u}} \right) - \overline{a^2} \nabla \cdot \overline{\mathbf{u}} = 0 \tag{9}$$

Subtracting it from Eq. 8 and neglecting second- and higher-order terms,

$$\frac{\partial^2 \phi}{\partial t^2} + 2\overline{\mathbf{u}} \cdot \nabla \frac{\partial \phi}{\partial t} + \overline{\mathbf{u}} \cdot (\nabla \overline{\mathbf{u}} \cdot \nabla \phi) + \frac{1}{2} \nabla \phi \cdot \nabla (\overline{\mathbf{u}} \cdot \overline{\mathbf{u}}) - \overline{a^2} \nabla^2 \phi - (a^2)' \nabla \cdot \overline{\mathbf{u}} \;=\; 0 \tag{10}$$

The fluctuating speed of sound squared is readily obtained from Eq. 5:

$$(a^2)' \;=\; -(\gamma - 1) \frac{\partial \phi}{\partial t} - (\gamma - 1) \overline{\mathbf{u}} \cdot \nabla \phi \;=\; -(\gamma - 1) \frac{\overline{D} \phi}{Dt} \tag{11}$$

while the mean value of the speed of sound squared is obtained by the mean terms of Eq. 5:

$$\overline{a^2} \;=\; a_\infty^2 - \frac{\gamma - 1}{2} \left(\overline{\mathbf{u}} \cdot \overline{\mathbf{u}} - U_\infty^2 \right) \tag{12}$$

Using these relations we arrive at the expression

$$\frac{\partial^2 \phi}{\partial t^2} + 2\overline{\mathbf{u}} \cdot \nabla \frac{\partial \phi}{\partial t} - a_\infty^2 \nabla^2 \phi \;=\; -E \tag{13}$$

with

$$E = \overline{\mathbf{u}} \cdot \nabla (\overline{\mathbf{u}} \cdot \nabla \phi) + \frac{1}{2} \nabla \phi \cdot \nabla (\overline{\mathbf{u}} \cdot \overline{\mathbf{u}}) + (\gamma - 1) \nabla \cdot \overline{\mathbf{u}} \frac{\overline{D} \phi}{Dt} + \frac{\gamma - 1}{2} \left(\overline{\mathbf{u}} \cdot \overline{\mathbf{u}} - U_\infty^2 \right) \nabla^2 \phi \tag{14}$$

The system of Eqs. 13-14 was first derived by Vaidya.[5] The term E represents "sources" that stem from mean flow gradients (first three terms) and the difference between ambient and local speed of sound squared (last term). We treat E as an error term and and evaluate its magnitude after solving the homogeneous version of Eq. 13. As a preliminary step, an order-of-magnitude assessment of the error term is offered in Section II.D.

Once the velocity potential is known, the acoustic pressure is obtained from the linearized momentum equation

$$p' \;=\; -\overline{\rho} \frac{\overline{D} \phi}{Dt} = -\overline{\rho} \left(\frac{\partial \phi}{\partial t} + \overline{\mathbf{u}} \cdot \nabla \phi \right) \tag{15}$$

C. Transformation

The mixed-derivative term on the left hand side of Eq. 13 can be eliminated via the time transformation introduced by Taylor:[7]

$$T \;=\; t + \frac{\overline{\Phi}}{a_\infty^2} \tag{16}$$

where $\overline{\Phi}$ denotes the velocity potential for the *mean* flow:

$$\overline{\mathbf{u}} \;=\; \nabla \overline{\Phi} \tag{17}$$

We proceed with the derivative transformations, noting that $\mathbf{x}$ and t are no longer independent.

$$\begin{aligned} \frac{\partial}{\partial t} \;&\rightarrow\; \frac{\partial}{\partial T} \\ \nabla \;&\rightarrow\; \nabla + \frac{\nabla \overline{\Phi}}{a_\infty^2} \frac{\partial}{\partial T} = \nabla + \frac{\overline{\mathbf{u}}}{a_\infty^2} \frac{\partial}{\partial T} \\ \nabla^2 \;&\rightarrow\; \nabla^2 + \frac{2}{a_\infty^2} \overline{\mathbf{u}} \cdot \nabla \frac{\partial}{\partial T} + \frac{\overline{\mathbf{u}} \cdot \overline{\mathbf{u}}}{a_\infty^4} \frac{\partial^2}{\partial T^2} \end{aligned} \tag{18}$$

Substituting in Eq. 13,

$$\left(1 + \frac{\overline{\mathbf{u}} \cdot \overline{\mathbf{u}}}{a_\infty^2} \right) \frac{\partial^2 \phi}{\partial T^2} - a_\infty^2 \nabla^2 \phi = -E \tag{19}$$

The second term inside the parenthesis is of order M^2 and can be absorbed into the error term such that

$$\frac{\partial^2\phi}{\partial T^2} - a_\infty^2\nabla^2\phi = -E' \tag{20}$$

with

$$E' = \overline{\mathbf{u}}\cdot\nabla(\overline{\mathbf{u}}\cdot\nabla\phi) + \frac{1}{2}\nabla\phi\cdot\nabla(\overline{\mathbf{u}}\cdot\overline{\mathbf{u}}) + (\gamma-1)\nabla\cdot\overline{\mathbf{u}}\frac{\overline{D}\phi}{Dt} + \frac{\gamma-1}{2}\left(\overline{\mathbf{u}}\cdot\overline{\mathbf{u}} - U_\infty^2\right)\nabla^2\phi + \frac{\overline{\mathbf{u}}\cdot\overline{\mathbf{u}}}{a_\infty^2}\frac{\partial^2\phi}{\partial t^2} \tag{21}$$

The redefined error, E', is written here in the original domain. Equation 20 is the inhomegeneous wave equation in the new time coordinate T. Taylor's transformation was used by Astley and Bain[6] towards the development of boundary-element methods acoustics in moving media. However, the step of including the term $\overline{\mathbf{u}}\cdot\overline{\mathbf{u}}/a_\infty^2$ (Eq. 19) in the error was not performed. It will be shown that this is a very significant contributor to the error of the cases investigated here. We also note recent work by Wolf and Lele[8] on BEM simulations in a potential flow, using point sources, that utilized Taylor's transformation.

D. Order-of-Magnitude Evaluation of Error Term

We follow an approach similar to Astley and Bain's[6] in evaluating the order of magnitude of the error terms in Eq. 21. The characteristic length scales of the mean flow and the acoustic field are denoted as L_M and L_A, respectively. The characteristic value of ϕ is denoted $[\phi]$. Dividing Eq. 20 by a_∞^2, the left hand side is of order $[\phi]/L_A^2$. The corresponding terms of the right hand side have the following orders:

$$\begin{aligned}
\frac{E_1'}{a_\infty^2} &= \frac{1}{a_\infty^2}\overline{\mathbf{u}}\cdot\nabla(\overline{\mathbf{u}}\cdot\nabla\phi) \;\sim\; M_\infty^2\frac{[\phi]}{L_A L_M}\\
\frac{E_2'}{a_\infty^2} &= \frac{1}{2a_\infty^2}\nabla\phi\cdot\nabla(\overline{\mathbf{u}}\cdot\overline{\mathbf{u}}) \;\sim\; M_\infty^2\frac{[\phi]}{L_A L_M}\\
\frac{E_3'}{a_\infty^2} &= \frac{1}{2a_\infty^2}(\gamma-1)\nabla\cdot\overline{\mathbf{u}}\frac{\overline{D}\phi}{Dt} \;\sim\; M_\infty^2\frac{[\phi]}{L_A L_M}\\
\frac{E_4'}{a_\infty^2} &= \frac{\gamma-1}{2a_\infty^2}\left(\overline{\mathbf{u}}\cdot\overline{\mathbf{u}} - U_\infty^2\right)\nabla^2\phi \sim\; M_\infty^2\frac{[\phi]}{L_A^2}\\
\frac{E_5'}{a_\infty^2} &= \frac{\overline{\mathbf{u}}\cdot\overline{\mathbf{u}}}{a_\infty^4}\frac{\partial^2\phi}{\partial t^2} \;\sim\; M_\infty^2\frac{[\phi]}{L_A^2}
\end{aligned} \tag{22}$$

Terms E_4' and E_5' vanish as $M_\infty^2 \to 0$, consistent with the framework of this theory. Terms E_1', E_2' and E_3' are small compared to the left hand side of Eq. 20 if $M_\infty^2 L_A/L_M \to 0$. Therefore, these error terms may become appreciable, even as $M_\infty^2 \to 0$, if $L_A/L_M >> 1$. Thus the approach may fail if the mean-flow scale is much smaller than the acoustic wavelength.

E. Harmonic Fields

1. *Governing Equation*

We now consider the harmonic time dependence $e^{-i\omega t}$. On applying the substitution

$$\phi(\mathbf{x},t) \;\rightarrow\; \phi(\mathbf{x},\omega)e^{-i\omega t}$$

the transformation of Eq. 16 yields

$$\phi(\mathbf{x},\omega)e^{-i\omega t} = \phi(\mathbf{x},\omega)\; e^{i\omega\Phi/a_\infty^2}e^{-i\omega T}$$

Applying to Eq. 20, it is evident that the transformed variable

$$\widetilde{\phi}(\mathbf{x},\omega) = \phi(\mathbf{x},\omega)\; e^{i\omega\overline{\Phi}/a_\infty^2} \tag{23}$$

satisfies the inhomogeneous Helholtz equation

$$\nabla^2\widetilde{\phi} + k^2\widetilde{\phi} \;=\; -\widetilde{E'} \tag{24}$$

Thus, in the frequency domain, the transformation applies only to the dependent variable. There are no coordinate or frequency transformations. Consequently, there is no transformation of the boundary condition on the surface as long as the surface is rigid, i.e., $\mathbf{u}' \cdot \mathbf{n} = 0$, where $\mathbf{n}$ is the unit normal on the surface.

The following sections develop solutions for the homogeneous version of Eq. 24. Once the homogeneous solution is obtained, an error assessment is conducted by computing E' in the frequency domain.

F. Boundary Element Method

Boundary integral equations[9] are central to solving acoustic scattering and radiation problems (Fig. 2). We discuss BIEs for the canonical wave equation as they the form the basis for scattering solvers. Flow effects can be introduced by applying the BIEs in the transformed domain.

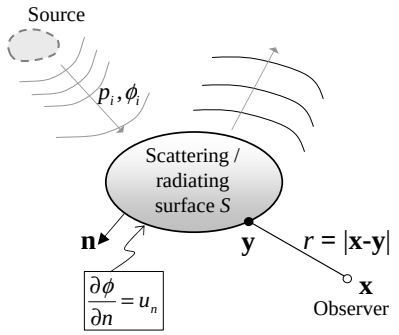

Figure 2. Acoustic scattering/radiation problem.

The BIE has exactly the same form for all acoustic scalar variables, although the surface boundary conditions may be different for each variable. The BIE for the acoustic potential is

$$c(\mathbf{x})\phi(\mathbf{x}) \;=\; \int_S \left[G(\mathbf{x}|\mathbf{y}) \frac{\partial \phi(\mathbf{y})}{\partial n} - \frac{\partial G(\mathbf{x}|\mathbf{y})}{\partial n} \phi(\mathbf{y}) \right] d^2\mathbf{y} \;+ \phi_i(\mathbf{x}) \tag{25}$$

G is the Green's function; $c(\mathbf{x})$ takes the values 1 in the exterior, 1/2 on the surface (assuming the surface is smooth), and 0 in the interior of the body; and subscript i denotes the incident field. The normal acoustic velocity on the surface is

$$u_n \;=\; \mathbf{u}' \cdot \mathbf{n} \;=\; \nabla\phi \cdot \mathbf{n} \;=\; \frac{\partial \phi}{\partial n} \tag{26}$$

For a rigid body, $u_n = 0$.

This study used a fast-multipole version of the boundary element method called FastBEM (Advanced CAE Research, LLC. See also Ref. 10). The size of the mesh elements that defined the scattering bodies was $\lambda/8$, where λ is the acoustic wavelength. The BEM solves the acoustic potential in the transformed domain. To obtain the acoustic pressure in the original domain with forward flight, the gradient of the acoustic potential must be known (Eq. 15). Additionally, to evaluate the error field, the bigradient (gradient of the gradient) and the Laplacian of the acoustic potential in the original domain must also be known. Two different sets of gradient evaluation schemes were used depending on whether the point of interest was a field point or a point on the body. Both sets of evaluation schemes required that additional field points surround the point of interest: six points for gradient and 18 for the bigradient. The gradient, bigradient, and Laplacian evaluation schemes at field points were based on second-order central differencing. For points on the body, these quantities were evaluated using forward differencing based on a localized axis centered on the mesh elements. The local axis was rotated such that all the additional field points lay outside the body and within the acoustic domain.

To demonstrate the accuracy of the BEM method, we treat the problem of monopole diffraction by a sphere (Fig. 6) and compare the computational prediction of the total (incident plus scattered) pressure field with the analytical solution of Morris.[11] Figure 3 plots the polar distribution of the magnitude of the total pressure at a radius $r = 3r_0$ centered at the sphere, for non-dimensional wavenumbers kr_0=5, 20, and 50. The match between BEM prediction and analytical solution is perfect at kr_0=5 and 20, and very good at $kr = 50$. This indicates that the BEM method, and the grid resolution selected for the scattering surface, perform satisfactorily for the predictions that follow.

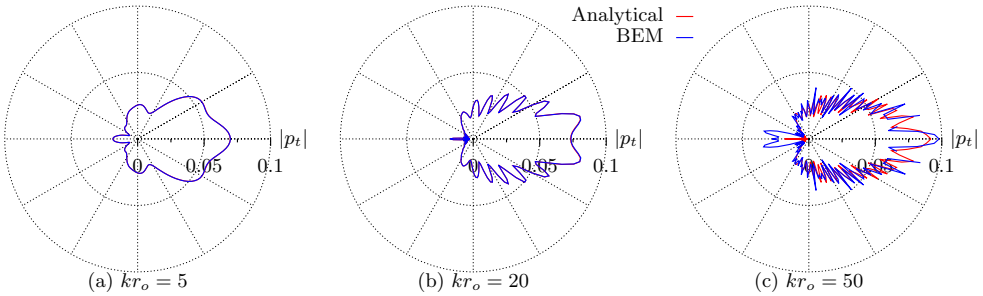

Figure 3. Comparison of analytical and computational predictions for the magnitude of the total pressure field for the problem of monopole diffraction by a sphere. a) $kr_0 = 5$**; b)** $kr_0 = 20$**; b)** $kr_0 = 50$**.**

III. Source Fields

We discuss the treatment of two types of sources used in the scattering problems of this study: the monopole and the wavepacket. The former is used for the canonical problem of sound diffraction by a sphere; the latter simulates the jet noise source and will be integrated with an aerodynamic surface.

A. Monopole

In the transformed domain, the monopole is a volume source/sink visualized as a uniformly-pulsating sphere with radius much smaller than the acoustic wavelength creating a disturbance in a still medium. Considering a harmonic monopole centered at $\mathbf{x}_s$, the acoustic potential is

$$\widetilde{\phi}_i(\mathbf{x}) = \frac{Q}{4\pi|\mathbf{x}-\mathbf{x}_s|} e^{ik|\mathbf{x}-\mathbf{x}_s|} \tag{27}$$

Once the scattered and total fields are computed in the transformed domain, the respective fields in the original domain are obtained by applying the inverse of the transformation of Eq. 23. The procedure is illustrated in Fig. 4.

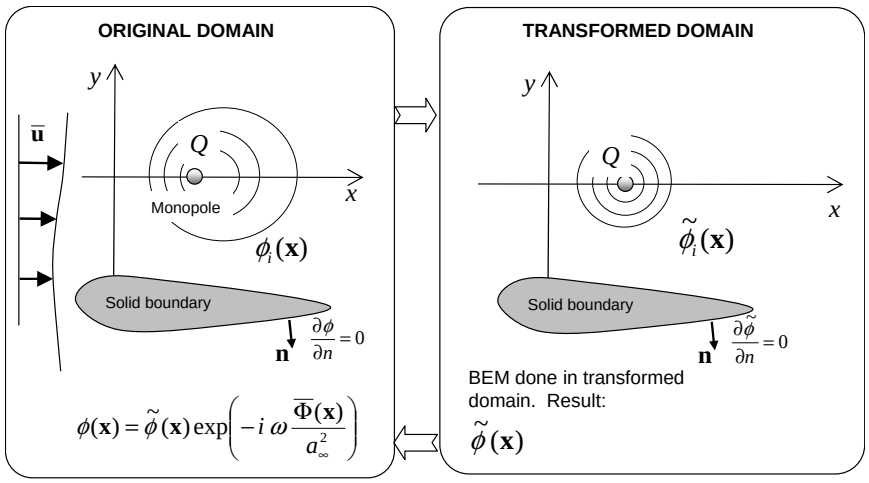

Figure 4. Transformation of the monopole field and its diffraction.

B. Wavepacket

At its most general interpretation, the wavepacket model is an application of Kirchhoff's integral theorem:[12] an acoustic field is prescribed on a surface, then it is propagated away from the surface using the wave

propagator. Here the surface is a cylinder of radius $r = r_0$. In the physical domain, the prescribed disturbance has the form

$$\phi_i(x, r_0) \;=\; \phi_0(x) e^{in\psi} \tag{28}$$

where ψ is the azimuthal angle, and n is the helical mode. In the transformed domain, using Eq. 23, the imposed disturbance becomes

$$\widetilde{\phi}_i(x, r_0) \;=\; \widetilde{\phi}_0(x) e^{in\psi} = \phi_0(x) e^{i\omega\overline{\Phi}/a_\infty^2}\; e^{in\psi} \tag{29}$$

The solution in the transformed domain is obtained by solving the canonical wave equation in polar coordinates:[13]

$$\widetilde{\phi}_i(x, r, \psi) \;=\; \frac{1}{2\pi} e^{in\psi} \int_{-\infty}^{\infty} \widehat{\widetilde{\phi}}_0(k_x) \frac{H_n^{(1)}(k_r r)}{H_n^{(1)}(k_r r_0)} e^{ik_x x} dk_x \tag{30}$$

where

$$k_r \;=\; (k_x^2 - k^2)^{1/2}, \quad -\frac{\pi}{2} < \arg(k_r) < \frac{\pi}{2} \tag{31}$$

Here $k = \omega/a_\infty$ is the acoustic wavenumber; $\widehat{()}$ denotes the spatial Fourier transform; k_x is the axial wavenumber; k_r is the radial wavenumber; and $H_n^{(1)}$ is the Hankel function of the first kind of order n. The solution is radiating for $|k_x| \le k$, for which k_r is real; and decaying for $|k_x| \ge k$, for which k_r is imaginary.

The spatial Fourier transform of $\widetilde{\phi}_0$ in Eq. 30 is tedious because it involves the velocity potential of the mean flow. However, if we make the assumption that, near $r = r_0$, the mean flow is uniform with velocity $\overline{\mathbf{u}} = U_0\mathbf{i}$, the mean velocity potential reduces to $\overline{\Phi} = U_0 x$ and the transformed acoustic potential simplifies to

$$\widetilde{\phi}_0(x) = \phi_0(x) e^{ikM_0 x}\; e^{in\psi}$$

with $M_0 = U_0/a_\infty$. Further, for a problem where the wavepacket is placed near a streamlined body, it is reasonable to approximate $M_0 \approx M_\infty$. Then we readily obtain

$$\widetilde{\phi}_i(x, r, \psi) \;=\; \frac{1}{2\pi} e^{in\psi} \int_{-\infty}^{\infty} \widehat{\phi}_0(k_x - kM_\infty) \frac{H_n^{(1)}(k_r r)}{H_n^{(1)}(k_r r_0)} e^{ik_x x} dk_x \tag{32}$$

This is the wavepacket incident field in the transformed domain. Once the scattered and total fields are computed, their respective fields in the original domain are obtained by reversing the transformation of Eq. 23. The process is illustrated in Fig. 5.

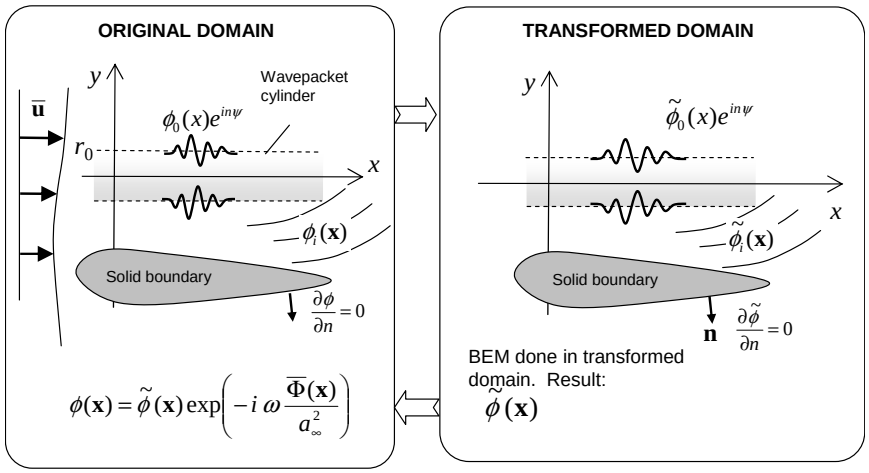

Figure 5. Transformation of the wavepacket field and its diffraction.

In this study the disturbance imposed on $r = r_0$ has the form

$$\phi_0(x') \;=\; \tanh(x'/b_1)^{p_1}\;\left[1 - \tanh(x'/b_2)^{p_2}\right] e^{i\alpha x'} \tag{33}$$

Here x' is a local axial coordinate that is related to the x-coordinate via $x = x' - x'_{max}$, where x'_{max} is the location of the peak amplitude of the radiating component of the wavepacket pressure. Equation 33, in combination with the $e^{-i\omega t}$ harmonic factor describes an amplifying-decaying wave traveling with convective velocity $U_c = \omega/\alpha$. The amplification is controlled by the width b_1 and power p_1, while the decay is controlled by the width b_2 and power p_2. Considering a given jet flow, the parameters α, b_1, b_2, p_1 and p_2 are determined by matching the directivity of the far-field sound intensity, at a given frequency, using the procedures in Ref. 4.

The wavepacket model of this study captures the far-field directivity of a separate-flow, bypass ratio 10 nozzle tested in our laboratory.[14] The jet diameter was $D_j = 0.0312$ m and the jet characteristic velocity was $U_j = 279$ m/s. Table 1 lists the wavepacket parameters. The Strouhal number is defined as $Sr = fD_j/U_j$.

Table 1. Wavepacket parameters

Sr	n	U_c/U_j	b_1/D_j	b_2/D_j	p_1	p_2
0.20	0	0.471	4.09	6.15	2.26	3.42
0.50	0	0.577	1.41	2.73	1.62	2.79
1.26	2	0.603	0.54	1.07	1.44	2.51

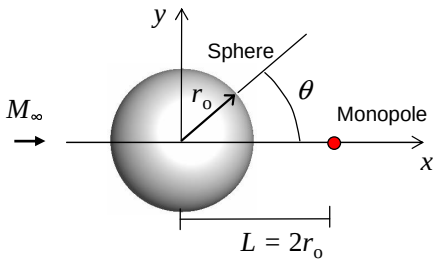

Figure 6. Setup of monopole and sphere.

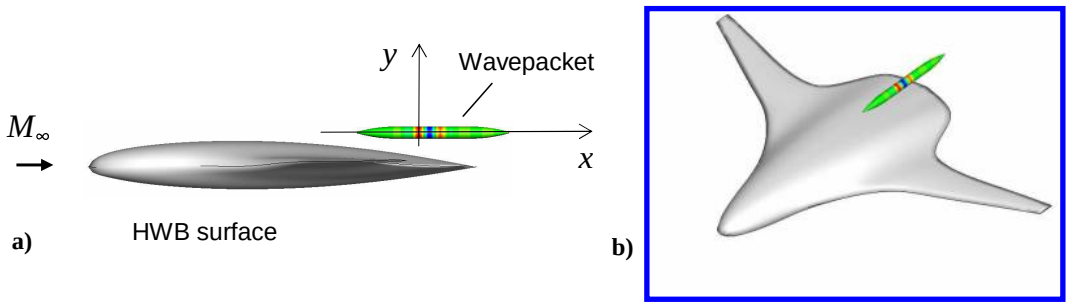

Figure 7. Setup of HWB-shaped surface and wavepacket. a) Side view; b) perspective view.

IV. Flow Fields

We study the effects of mean flow on the acoustics of two problems: the diffraction of monopole emission by a sphere, shown in Fig. 6; and the diffraction of wavepacket emission by an HWB-shaped boundary, shown in Fig. 7. In both instances the freestream is uniform with Mach number M_∞. For the monopole and sphere problem, the monopole is situated two radii downstream of the center of the sphere. The coordinate system in this problem is centered with the sphere. For the wavepacket and HWB problem, the surface shape is patterned after the N2AEXTE HWB[4] without vertical fins and with a symmetrical cross-section, with thickness-to-chord ratio of 12% on the symmetry plane. The wing is placed at zero angle of attack. The wavepacket is on the symmetry plane and the coordinate system is centered with the wavepacket, the origin $x = 0$ signifying the peak of the radiating pressure on the wavepacket surface (see Eq. 33). The wing trailing

edge is located at $x/s = 0.111$, y/s=0.062, where s is the wing span. The wavepacket cylinder diameter is $D_j/s = 0.043$.

For both the sphere and HWB bodies the flow field is obtained by the solution to Laplace's equation $\nabla^2\overline{\Phi} = 0$ subject to the boundary condition on the body. In other words, the flow solution is inherently incompressible although we allow the freestream Mach number M_∞ to take a finite value. For a given subsonic M_∞, the departure from the exact solution is expected to be worse for the sphere than for the HWB because the latter is a streamlined body. This departure is not included in the present error assessment.

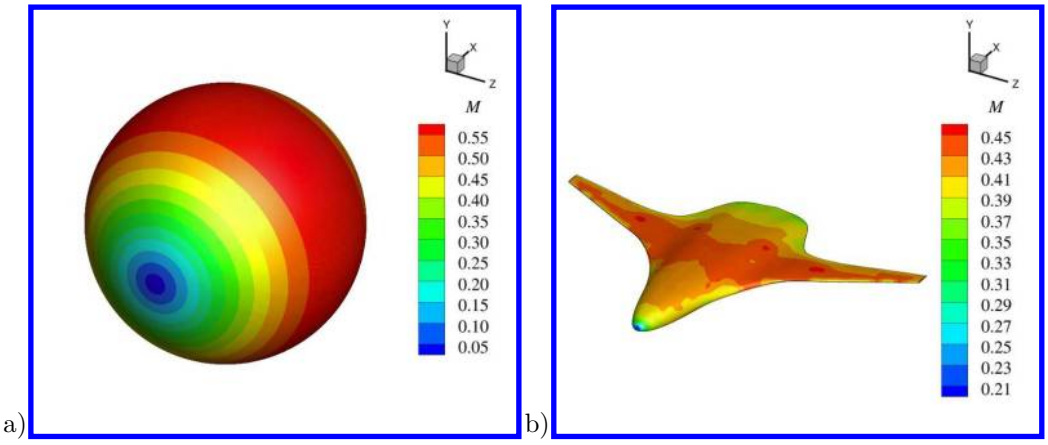

Figure 8. Surface Mach number contours for $M_\infty = 0.4$. a) Sphere; b) HWB-shaped surface.

The flow field around the sphere was obtained using the analytical incompressible potential-flow solution. The mean flow around the HWB surface was computed using the potentialFoam solver of the OpenFOAM computational fluid dynamics package. The potentialFoam solver is an incompressible potential flow solver wherein the discretized linear system of equations is solved iteratively to a convergence tolerance of 10^{-6} using a preconditioned conjugate gradient method. The diagonal incomplete-Cholesky preconditioner for symmetric matrices was used. The computational domain had dimensions $20s$, $10s$, and $20s$ in the x, y, and z directions, respectively, and was centered at the trailing edge on the symmetry plane. The domain was discretized into an unstructured field mesh composed of 357128 tetrahedral volume cells using the NETGEN algorithm. The grid resolution was $0.015s$ on the surface and gradually increased to $0.5s$ at the boundaries of the domain. At the inlet of the domain the velocity was prescribed at $\overline{\mathbf{u}} = (1, 0, 0)$ and at the outlet the pressure was fixed at $\bar{p} - p_a = 0$, where p_a is the ambient pressure. The boundary conditions on the surface was $\overline{\mathbf{u}} \cdot \mathbf{n}$=0. Symmetry conditions were applied across the xy and xz planes. Once the flow field was computed, the values of mean velocity, mean velocity gradient, and gradient of the squared mean velocity magnitude were interpolated onto the desired field points.

The incompressible nature of the mean-flow solution means that $\nabla \cdot \overline{\mathbf{u}} = 0$, thus the third error term in Eq. 22 is theoretically equal to zero. However, to account for the finite speed of sound of the pseudo-compressible flow solution employed here, the divergence of the mean velocity field was computed from Eq. 9. This is expected to give a more realistic estimate of the E_3' error term. Nevertheless, this term is very small as will be shown in the results of Section VI.

V. Mach Number Effect on Total Pressure Field

We discuss the effect of the flight Mach number M_∞ on the diffraction of sound for the two problems defined Section IV. The total pressure field is the complex addition of the incident and scattered pressure fields, $p_t = p_i + p_s$.

A. Monopole and Sphere

Figure 9 presents polar plots of the magnitude of the total pressure, $|p_t|$, for Mach numbers M_∞=0, 0.1, 0.2, 0.4, and 0.6, and for non-dimensional wavenumbers kr_0 =5, 20, and 50. The pressure is evaluated on the circle $r = 3r_0$ centered at the center of the sphere. For all the wavenumbers, increasing M_∞ results in a

compaction of the aft-emitted radiating noise source region, with a narrow region of upstream amplification. The latter is more pronounced at high frequency.

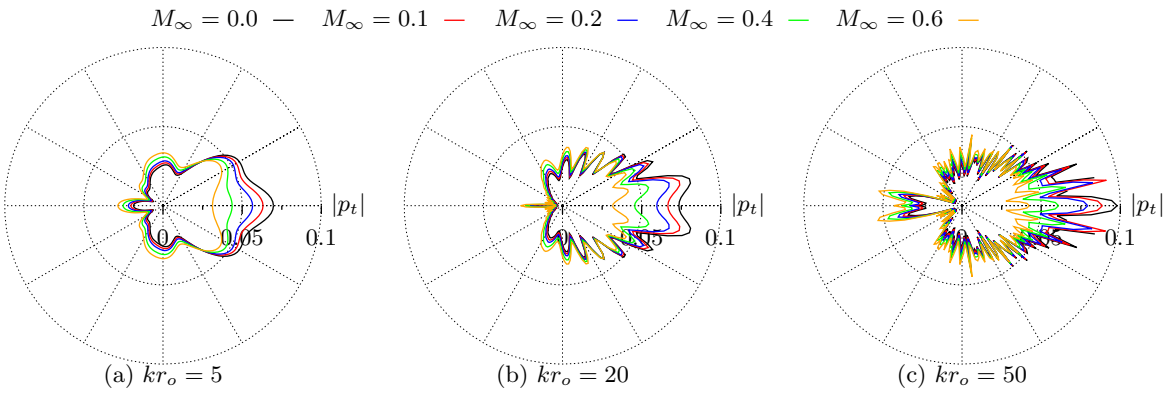

Figure 9. Effect of Mach number on the magnitude of the total pressure field for the problem of monopole diffraction by a sphere. a) $kr_0 = 5$**; b)** $kr_0 = 20$**; c)** $kr_0 = 50$**.**

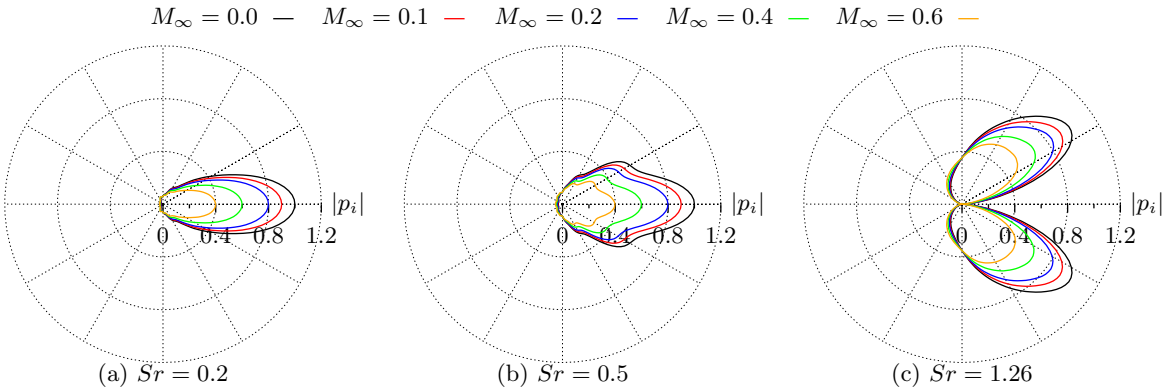

Figure 10. Effect of Mach number on the magnitude of the incident pressure field for the wavepacket source. a) $Sr = 0.2$**; b)** $Sr = 0.5$**; c)** $Sr = 1.26$**.**

B. Wavepacket and HWB Surface

We first examine the effect of freestream Mach number on the wavepacket incident pressure field. Figure 10 presents polar plots of the magnitude of the incident pressure, $|p_i|$, for Mach numbers M_∞=0, 0.1, 0.2, 0.4, and 0.6, and Strouhal numbers Sr =0.2, 0.5, and 1.26. The pressure is evaluated on the circle $r = 2.5s$ centered at the wavepacket origin. At low frequency the wavepacket is beaming radiation downstream. With increasing frequency, the polar angle of peak emission increases from the downstream axis. We note a trend of weakening of the source with increasing Mach number across all the Strouhal numbers. The decrease in the relative Mach number of the wavepacket instability, manifested in the argument $k_x - kM_0$ of the source term in Eq. 32, results in a reduction in the radiated energy. Reference 3 elaborates more on this phenomenon.

We now turn our attention to the total pressure field, plotted in Fig. 11 for the same conditions as in Fig. 10. The skewed distributions indicate attenuation in the downward direction (due to shielding from the HWB surface) and amplification in the upward reduction (due to reflection from the surface). The effect of increasing M_∞ is to weaken the distributions and to increase the downward attenuation, particularly at high frequency. Comparing the incident (Fig. 10) and total (Fig. 11) pressure distributions at $Sr = 1.26$, we note

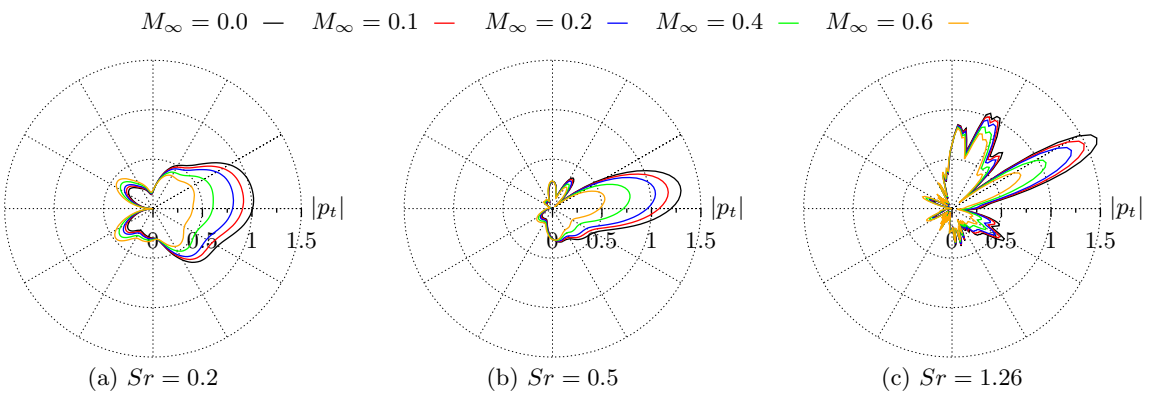

(a) $Sr = 0.2$ (b) $Sr = 0.5$ (c) $Sr = 1.26$

Figure 11. Effect of Mach number on the magnitude of the total pressure field for the problem of wavepacket diffraction by a HWB-shaped surface. a) $Sr = 0.2$**; b)** $Sr = 0.5$**; c)** $Sr = 1.26$**.**

that increasing M_∞ attenuates the downward (shielded) pressure much more than the upward (reflected) pressure. This is a consequence of the compaction of the radiating source, which increases the effectiveness of the HWB surface to shield downward-emitted noise.

VI. Error Assessment

The full error term in the physical domain is given by Eq. 21. Its harmonic form is

$$\begin{aligned} E' \;&= \overline{\mathbf{u}} \cdot \nabla(\overline{\mathbf{u}} \cdot \nabla\phi) + \frac{1}{2}\nabla\phi \cdot \nabla(\overline{\mathbf{u}} \cdot \overline{\mathbf{u}}) + (\gamma - 1)\nabla \cdot \overline{\mathbf{u}}\,(-i\omega\phi + \overline{\mathbf{u}} \cdot \nabla\phi) \\ &+ \frac{\gamma - 1}{2}\left(\overline{\mathbf{u}} \cdot \overline{\mathbf{u}} - U_\infty^2\right)\nabla^2\phi + \overline{\mathbf{u}} \cdot \overline{\mathbf{u}}\, k^2\phi \end{aligned} \tag{34}$$

It is compared to the harmonic form of the left hand side of Eq. 13

$$\omega^2\phi - 2i\omega\overline{\mathbf{u}} \cdot \nabla\phi - a_\infty^2\nabla^2\phi$$

whose homogeneous solution was obtained using the variable transformation and the BEM described in Section II. The magnitude of the left hand side of Eq. 13 scales with $\omega^2|\phi|$. Therefore, we compare $|\phi|$ to $|E'|/\omega^2$. To make the comparison as conservative as possible, the magnitude of the acoustic potential and the evaluation of the error term are based on the scattered acoustic potential ϕ_s. The error assessment is done in the "far field" and on the scattering surface.

A. Far-Field Evaluation

1. *Monopole and Sphere*

The far-field evaluation was done on the radius $r = 3r_0$ around the center of the sphere. Figure 12 presents polar plots of $|E'/\omega^2|$ at various freestream Mach numbers and compares them to the distribution of $|\phi_s|$. The comparisons are made at non-dimensional wavenumbers $kr_0 = 5$, 20, and 50. For $M_\infty \leq 0.2$ the error term is very small. It becomes appreciable at $M_\infty = 0.4$ where it can be as strong as $\sim 0.2|\phi_s|$. At $M_\infty = 0.6$ it dominates in the downstream and upstream directions. These trends hold for all the frequencies investigated.

It is instructive to examine the individual components of the far-field error, as broken down in Eq. 22. Figure 13 plots the magnitudes of the error components at $M_\infty = 0.6$ versus polar angle for kr_0=0.5 and kr_0 =50. The magnitudes are normalized by the maximum value of the scattered field on $r = 3r_0$, $|\phi_s|_{max}$. Note that the error contributions are coherent fields, so the sum of their magnitudes squared does not equal the total magnitude squared. For both frequencies the principal contributions come from terms E_1' and E_5', the former dominating at small polar angles and the latter becoming prominent for $\theta \geq 70°$. Term E_1'

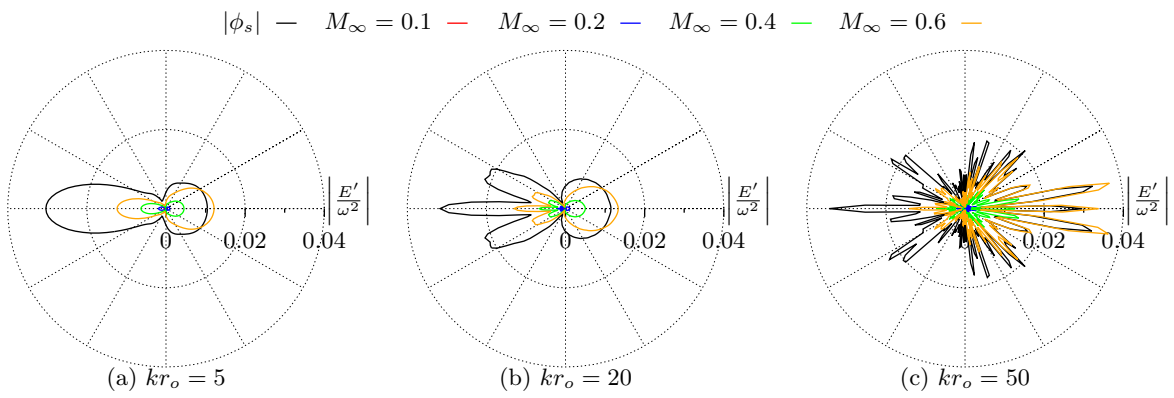

Figure 12. Magnitude of the overall far-field error $|E|/\omega^2$ compared to the magnitude of the scattered field $|\phi_s|$ for the problem of monopole diffraction by a sphere. a) $kr_0 = 5$; b) $kr_0 = 20$; b) $kr_0 = 50$.

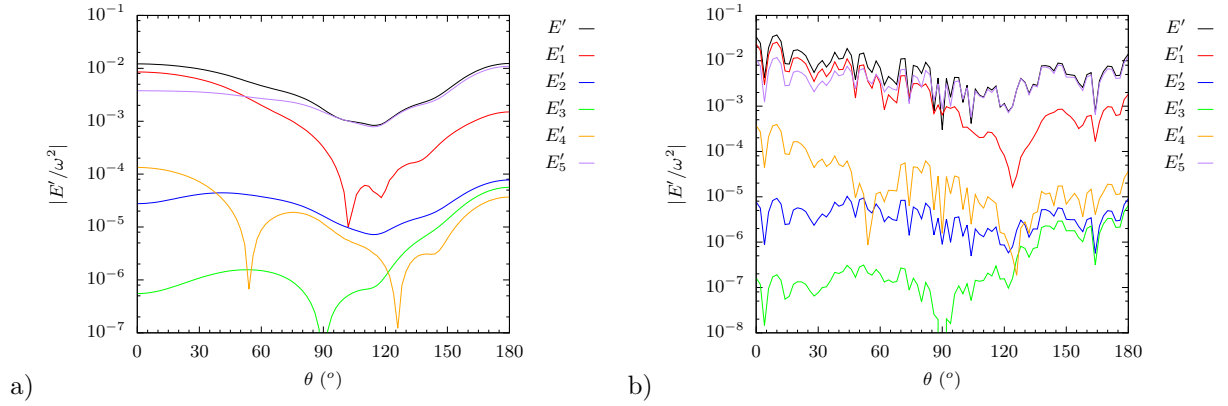

Figure 13. Magnitudes of individual far-field error components at $M_\infty = 0.6$ for the problem of monopole diffraction by a sphere. a) $kr_0 = 0.5$; b) $kr_0 = 50$.

involves the gradient of M whereas terms E'_2 and E'_3 involve gradients of M^2; it is thus expected that E'_1 will dominate the components that involve mean-flow gradients in Eq. 22. Contribution E'_5 arises from the transformation of Section II.C ($\mathbf{u} \cdot \mathbf{u}/a_\infty^2$ term in Eq. 19) and is directly proportional to M^2. In contrast, term E'_4 scales with $M^2 - M_\infty^2$ and is thus of lower overall magnitude. The error component breakdown seen in Fig. 13 is similar at the lower Mach numbers of this study.

2. Wavepacket and HWB

The far-field evaluation was done on the radius $r/s = 2.5$ centered at the wavepacket origin. Figure 14 plots $|E'/\omega^2|$ at various freestream Mach numbers with comparison to $|\phi_s|$, at Strouhal numbers $Sr = 0.2$, 0.5, and 1.26. The error is very small for $M_\infty \leq 0.2$, and becomes appreciable at $M_\infty \geq 0.4$. At $M_\infty = 0.4$ the error is on the order of $0.3|\phi_s|$, similar to the error for the sphere and monopole problem. At $M_\infty = 0.6$ the error is large and comparable to the scattered acoustic field. The magnitudes of the error components for $M_\infty = 0.6$, plotted versus polar angle, are shown in Fig. 15. The trends are similar as for the monopole and sphere problem (Fig. 13). Terms E'_1 and E'_5 dominate the error, the former impacting the small angles and the latter the large angles.

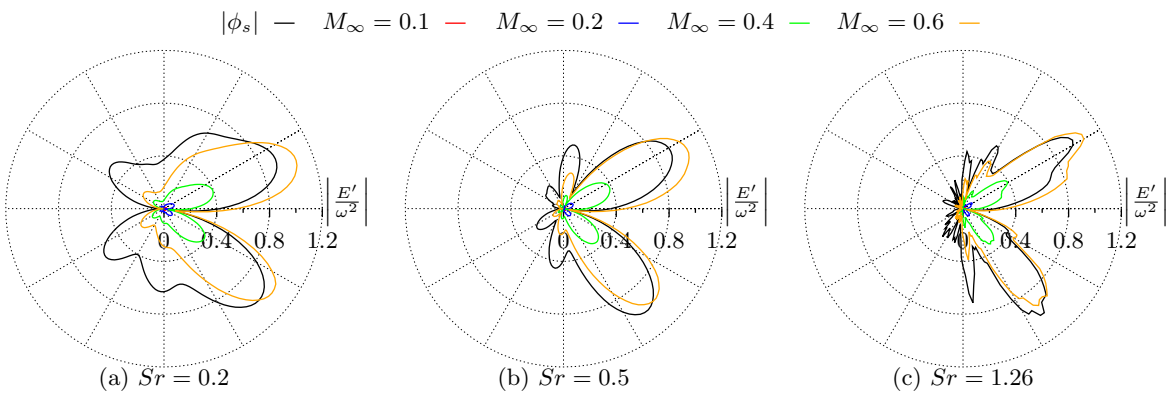

Figure 14. Magnitude of the overall error $|E|/\omega^2$ compared to the magnitude of the scattered field $|\phi_s|$ for the problem of wavepacket diffraction by a HWB-shaped surface. a) $Sr = 0.2$; b) $Sr = 0.5$; c) $Sr = 1.26$.

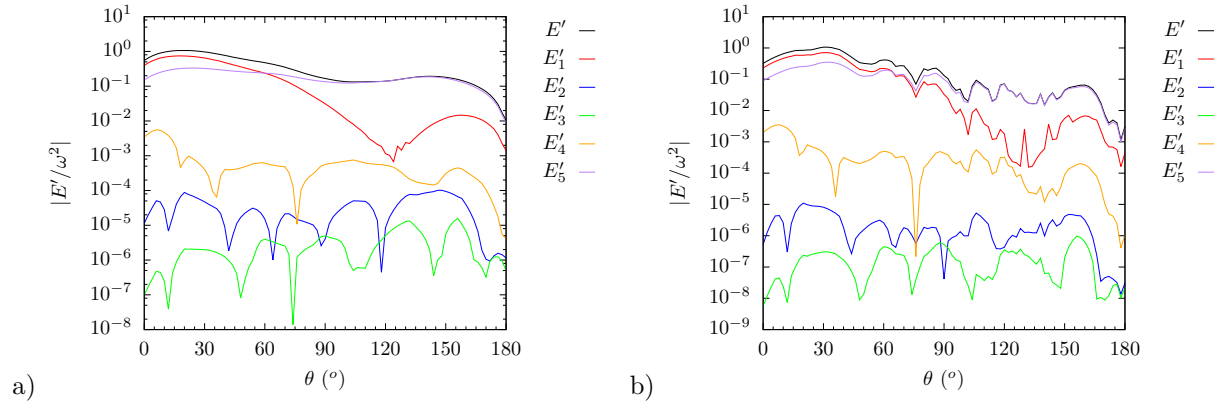

Figure 15. Magnitudes of individual far-field error components at $M_\infty = 0.6$ for the problem of wavepacket diffraction by a HWB-shaped surface. a) $Sr = 0.2$; b) $Sr = 1.26$.

B. Surface Evaluation

1. *Monopole and Sphere*

The error assessment was done on the surface of the sphere on the symmetry plane. Results are plotted against the polar angle θ defined with respect to the downstream axis. Figure 16 compares the magnitude of the overall error to the magnitude of the scattered acoustic field, all quantities being normalized by $|\phi_s|_{max}$. At low frequency ($kr_0 = 5$) the error for $M \geq 0.2$ is comparable or higher than the minimum value of $|\phi_s|$, which occurs near $\theta = 90°$. For $kr_0 \geq 5$ the error is uniformly lower than $|\phi_s|$, even for the highest Mach number investigated of 0.6. For $M_\infty \leq 0.4$ the error is about one order of magnitude lower than the magnitude of the scattered acoustic field.

The breakdown of the error terms for $M_\infty = 0.6$ is plotted in Fig. 17. At low frequency, the contributions are of comparable magnitude, except for E'_3 which is mostly lower than the other terms. At high frequency there is a clear separation of contributions with E'_5 dominating, as was seen in the far-field results. Results for the lower Mach numbers of this study are similar.

2. *Wavepacket and HWB*

The surface error evaluation was done at field points on the symmetry plane and at distance of $0.01s$ from the surface, as depicted in Fig. 18. The error and its components are plotted versus the coordinate η along the evaluation contour. The locations of the trailing edge (TE), wavepacket origin (WP), and leading edge

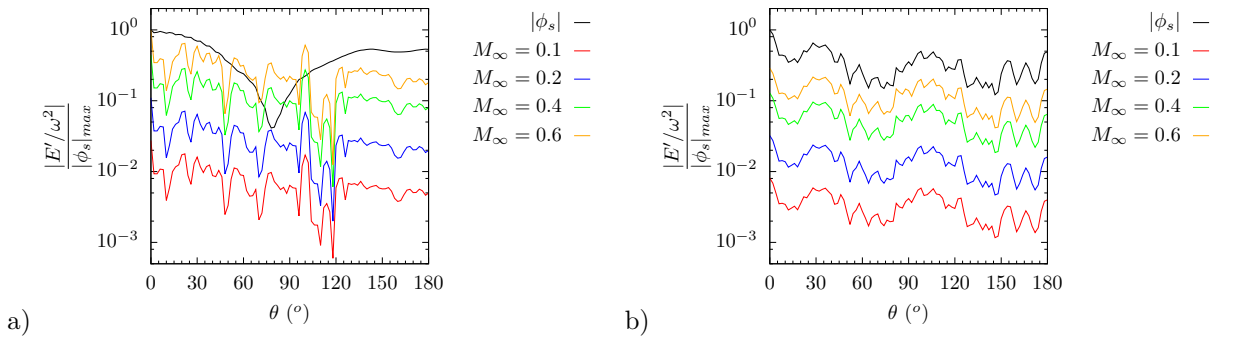

Figure 16. Magnitude of the overall surface error $|E|/\omega^2$ compared to the magnitude of the scattered field $|\phi_s|$ for the problem of monopole diffraction by a sphere. a) $kr_0 = 5$; b) $kr_0 = 50$.

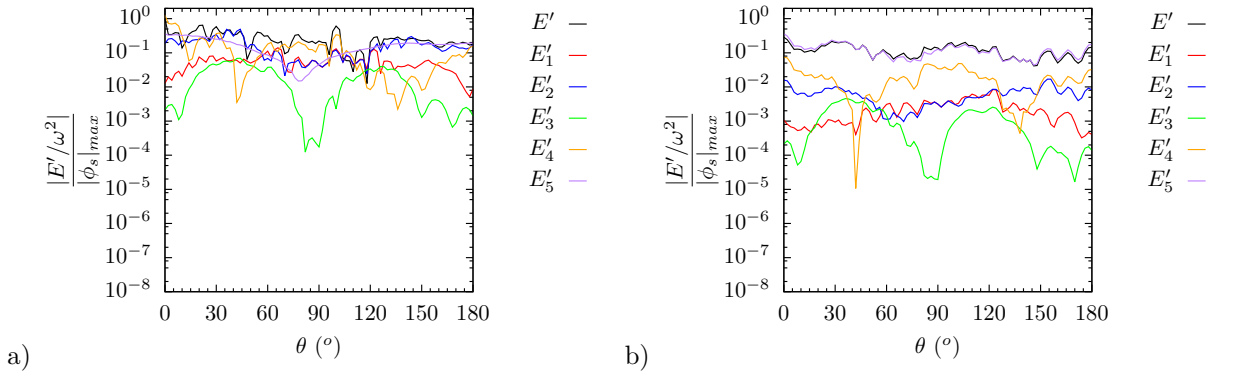

Figure 17. Magnitudes of individual surface error components at $M_\infty = 0.6$ for the problem of monopole diffraction by a sphere. a) $kr_0 = 0.5$; b) $kr_0 = 50$.

(LE) are identified on the plots. Figure 19 plots the surface distributions of the magnitudes of the scattered field and of the overall error for different Mach numbers and for $Sr = 0.2$ and 1.26. For both frequencies the error is uniformly smaller than the scattered field. For $M_\infty \leq 0.4$, the error is at least one order of magnitude smaller than the magnitude of the scattered field. The corresponding error components are plotted in Fig. 20, where we note a clear dominance of the E'_5 term. In contrast to the sphere problem (Fig. 17), the mean flow gradients in the HWB problem are weak and therefore the leading M^2-dependent term clearly dominates.

Figure 18. Surface evaluation of error for HWB and wavepacket problem.

C. Trends versus Mach Number

The magnitude of the overall error in the far field is now plotted versus freestream Mach number for different polar directions. The error is normalized by the magnitude of the scattered field in the same direction. Figure 21 presents the results for the sphere and monopole problem at $kr_0 = 0.5$ and 50. Figure 22 shows the analogous trends for the wavepacket and HWB problem for $Sr = 0.2$ and 1.26. In both problems the error scales approximately with M_∞^2, as expected from the scaling arguments of Section II.D. For the sphere and monopole problem the relative error is more pronounced in the downstream ($\theta = 0°$) and upstream ($\theta = 180°$) directions, and is weaker by factor of ~ 2 in the 90° direction. This difference amplifies with increasing frequency. At $M_\infty = 0.2$, the relative error is roughly 5%. The wavepacket and HWB problem

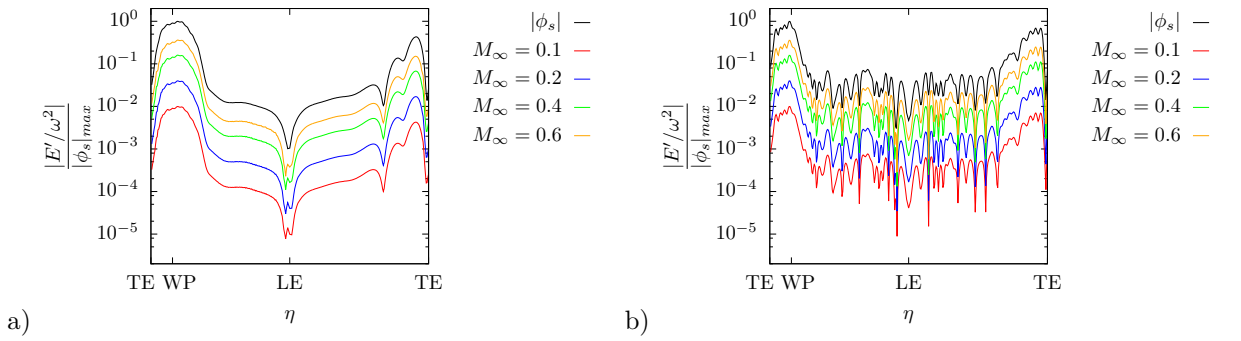

Figure 19. Magnitude of the overall surface error $|E|/\omega^2$ compared to the magnitude of the scattered field $|\phi_s|$ for the problem of wavepacket diffraction by a HWB surface. a) $Sr = 0.2$; b) $Sr = 1.26$.

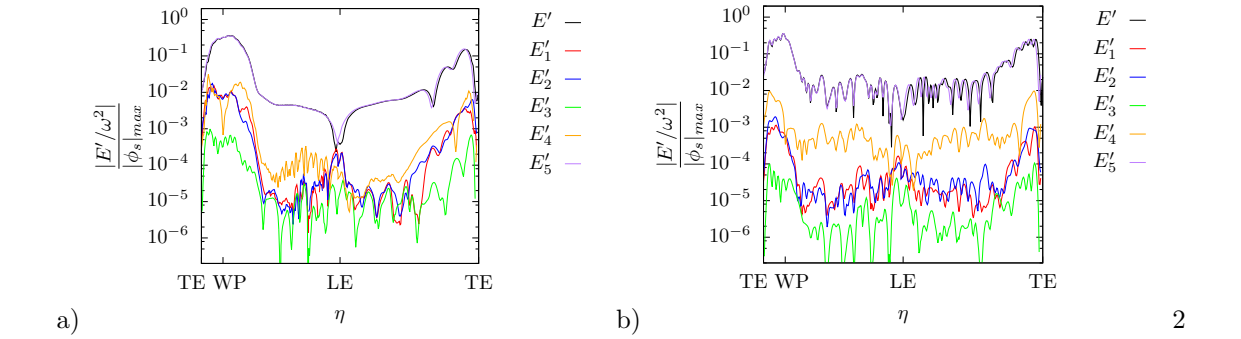

Figure 20. Magnitudes of individual surface error components at $M_\infty = 0.6$ for the problem of wavepacket diffraction by a HWB surface. a) $Sr = 0.2$; b) $Sr = 1.26$.

exhibits similar trends, with the error being minimized at $\theta \sim 90°$ and the magnitude of the relative error being ~ 5 % at $M_\infty = 0.2$.

VII. Conclusion

Prediction of sound propagation in a potential mean flow is possible by using solvers of the canonical wave equation in conjunction with a variable transformation that reduces the problem to an analogous static problem. This approach was applied here to an extended source that simulates jet noise - the wavepacket - and its diffraction by a surface that resembles the hybrid-wing-body (HWB) airplane. In addition, the canonical problem of monopole diffraction by a sphere was addressed.

The investigation assessed the effects of mean flow on the incident and diffracted fields, and provided a methodical assessment of the errors that arise from the transformations. The overall effect of the mean flow is a compaction of the downstream extent of the noise source, a trend that benefits noise shielding. The error of the transformation is on the order of 5% for $M_\infty = 0.2$ and 20% for $M_\infty = 0.4$. Of the error components, those which scale directly with the mean Mach number M and its gradient are dominant. Terms involving the gradient of M^2 are much less significant.

As pointed out in Section II.D, the danger of the transformation approach studied here is that it may fail if the mean flow scale is much smaller than the acoustic length scale, even at low Mach number. With the possible exception of the sphere and monopole problem at low frequency (Fig. 16a), this risk has not materialized here. The risk appears particularly low when the problem involves a streamlined aerodynamic body, like the HWB-shaped surface of this study.

References

[1]Tinetti, A. and Dunn, M., "Aeroacoustic Noise Prediction Using the Fast Scattering Code," AIAA 2005-3061, May 2005.

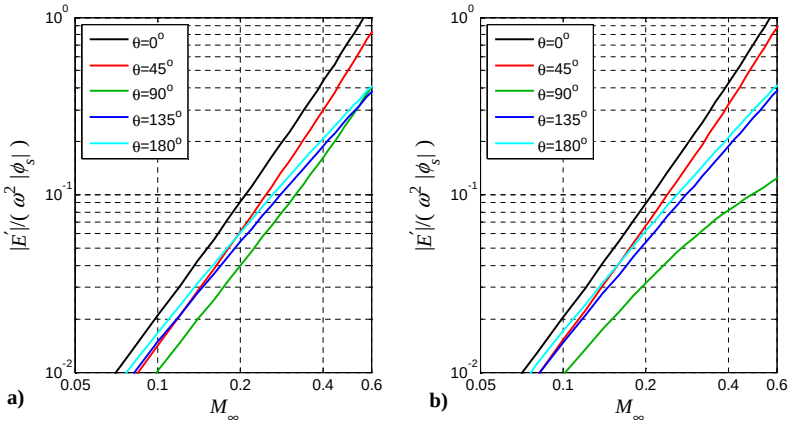

Figure 21. Magnitude of overall error, normalized by magnitude of scattered field, versus Mach number for different polar angles. Sphere and monopole problem at a) $kr_0 = 0.5$ and b) $kr_0 = 50$.

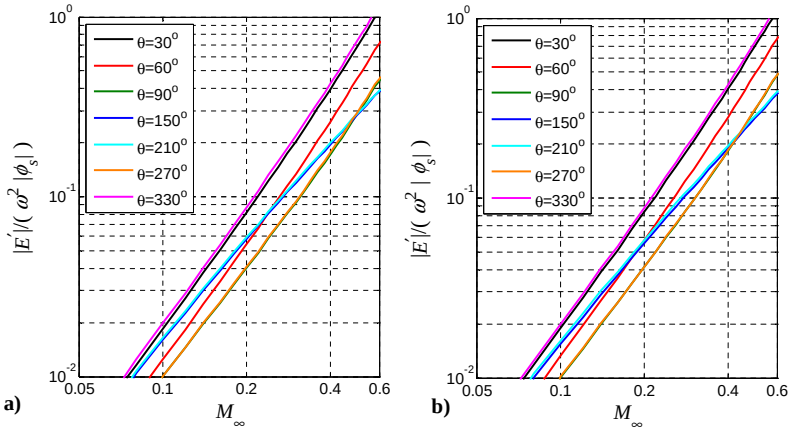

Figure 22. Magnitude of overall error, normalized by magnitude of scattered field, versus Mach number for different polar angles. HWB and wavepacket problem at a) $Sr = 0.2$ and b) $Sr = 1.26$.

[2]Bogey, C., Bailly, C., and Juve, D., "Computation of Flow Noise Using Source Terms," *AIAA Journal*, Vol. 40, No. 2, 2002, pp. 235–243.

[3]Papamoschou, D. and Mayoral, S., "Modeling of Jet Noise Sources and their Diffraction with Uniform Flow," AIAA 51st Aerospace Sciences Meeting, Jan. 2013.

[4]Papamoschou, D., "Prediction of Jet Noise Shielding," AIAA 2010-0653, Jan. 2010.

[5]Vaiyda, P., "Propagation of Sound in Flows Containing Mean Flow Gradients," AIAA 1981-1987, May 1981.

[6]Astley, R. and Bain, J., "A Three-Dimensional Boundary Element Scheme for Acoustic Radiation in Low Mach Number Flows," *Journal of Sound and Vibration*, Vol. 109, Sept. 1986, pp. 445–465.

[7]Taylor, K., "A Transformation of the Acoustic Equation with Implications for Wind-Tunnel and Low- Speed Flight Tests," *Proceedings of the Royal Society of London*, Vol. 363, No. 1713, Nov. 1978, pp. 271–281.

[8]Wolf, W. and Lele, S. K., "Fast Acoustic Scattering Simulations with Non-Uniform Potential Flow Effects," AIAA 2010-3712, June 2010.

[9]Wu, T., *Boundary Element Acoustics*, WIT Press, Boston, 2000.

[10]Liu, Y., *Fast Multipole Boundary Element Method - Theory and Applications in Engineering*, Cambridge University Press, Cambridge, 2009.

[11]Morris, P., "Scattering of Sound from a Spatially Distributed, Spherically Symmetric Source by a Sphere," *Journal of Acoustic Society of America*, Vol. 98, No. 6, Dec. 1995, pp. 3536–3539.

[12]Lyrintzis, A. and Mankbadi, R., "Prediction of the Far-Field Jet Noise Using Kirchhoff's Formulation," *AIAA Journal*, Vol. 34, Feb. 1996, pp. 413–416.

[13]Morris, P., "A Note on Noise Generation by Large Scale Turbulent Structures in Subsonic and Supersonic Jets," *International Journal of Aeroacoustics*, Vol. 8, No. 4, 2009, pp. 301–316.

[14]Papamoschou, D. and Mayoral, S., "Jet Noise Shielding for Advanced Hybrid Wing-Body Configurations," AIAA 2011-912, Jan. 2011.